


Research Article

Numerical Approach for Nonlinear Dynamics Simulation of Belt-Pulley XY Positioning Mechanism

M. R. Homaeinezhad*, M. M. Ebrahimi 

Faculty of Mechanical Engineering, K. N. Toosi University of Technology, Tehran, Iran
E-mail: mrhomaeinezhad@kntu.ac.ir

Received: 1 March 2024; **Revised:** 19 April 2024; **Accepted:** 30 April 2024

Abstract: In this article, the kinematics and dynamics of the CoreXY mechanism are explored, taking into account the motion of the collar plate. Within such mechanisms, the role of friction in the system dynamics is emphasized, necessitating its careful consideration during the derivation of equations. Friction, manifesting in both static and kinetic forms, can lead to the creation of dead zone regions in the system's operations. These zones are thoroughly discussed in this paper, and friction is accurately computed in various modes across the system components. Among the significant factors contributing to the creation of dead zones are the tension forces within the belts, whose effects on the mechanical dynamics are also meticulously examined. The impact of dead zones on the system dynamics is revealed through simulation results of the dynamic equations, shedding light on the various scenarios in which actuator inputs fall within or outside these dead zone regions. By employing the equations derived from this article, a comprehensive insight can be gained into the prevalent practice of modeling friction-exposed systems, along with a thorough understanding of the dynamic behavior of the CoreXY mechanism.

Keywords: nonlinear dynamics, XY positioning mechanism, varying (dynamic) dead zone, numerical simulation technique, CoreXY mechanism, belt driven system, static/dynamic friction, permanent magnet DC motor

1. Introduction

1.1 Overview

The CoreXY mechanism's significance is underscored by its ability to deliver unparalleled precision and accuracy. Its synchronized belt arrangement ensures minimal backlash and positional errors, resulting in finer and more detailed prints and cuts. The efficiency of this mechanism lies in its rapid and smooth movement, made possible by coordinated motor control and parallel belt paths, thereby reducing production times and enhancing Computer Numerical Control (CNC) machining operations. Moreover, the CoreXY design's focus on reduced inertia contributes to quicker acceleration and deceleration, ultimately translating into faster overall speeds. This harmonious movement also mitigates vibrations and sudden shifts, ensuring consistent layer heights in 3D printing and achieving precise cuts in CNC machining. The CoreXY mechanism's versatility finds application in an array of industries that demand exacting movement control. In the realm of 3D printing, it facilitates the creation of intricate designs, reduces vibrations for improved layer adhesion, and expedites the production of detailed prints. CNC machining benefits from its

precision, enabling intricate tasks such as milling, engraving, and cutting. Industries engaged in prototyping and rapid manufacturing capitalize on CoreXY's accuracy for crafting functional prototypes and small-scale production runs. From high technology industries, where intricate components meet stringent quality benchmarks, to the healthcare sector, which requires precision in medical devices, CoreXY mechanisms offer reliable performance. Despite its transformative potential, the mathematical modeling of the CoreXY mechanism presents a set of intricate challenges. Its complex kinematic structure gives rise to nonlinear relationships between motor inputs and positional outcomes, necessitating meticulous derivation of accurate mathematical expressions. Cross-axis coupling introduces further complexity, requiring the consideration of interactions between the x and y axes for precise modeling. Ensuring proper synchronization of belts and accounting for their behavior, along with belt stretch and tension, is paramount for an accurate model. Incorporating motor dynamics, friction, wear, and discretization into the model demands a comprehensive understanding of mechanical and dynamic behavior. This paper presents a comprehensive study that delves into the intricate domain of kinematics and dynamics modeling of the CoreXY mechanism. Notably, the analysis takes into account the frictional states of the mechanism's components and explores the unique dead zone phenomena, revealing its dependence on the tension forces exerted on voltage inputs and torques. By investigating the system's behavior under varying scenarios and inputs, a deeper understanding of its performance characteristics is sought, along with insights for future control strategies that have the potential to facilitate the operational landscape of the CoreXY mechanism.

The realm of mechanical systems and precision engineering has been invigorated by a series of pioneering studies, each embarking on a distinct journey to unravel the intricacies of friction compensation, dynamic control, and advanced motion mechanisms. Through meticulous investigations and innovative approaches, these studies have contributed to the evolution of mechanical design and positioning technologies, pushing the boundaries of performance, accuracy, and efficiency. One notable avenue of exploration delves into the realm of friction compensation, a vital pursuit in the following of enhanced precision and control. In study [1], researchers delved into the nuances of friction within a planar slider, employing parameter estimation techniques to develop a friction model. This model was further integrated with a Proportional-Integral-Derivative (PID) controller to achieve impeccable position tracking accuracy, offering insights into the dynamic mitigation of frictional forces. In the expansive realm of additive manufacturing, study [2] presents a paradigm-shifting endeavor centered around a large-scale 3D printing device. This innovation harnesses the CoreXY arrangement, leveraging its advantages through the application of simple kinematic equations. This approach not only amplifies printing accuracy but also lays the foundation for streamlined and efficient printing processes on a grand scale. The pursuit of dynamic control and precision is further illuminated in study [3], where the concept of adaptive fuzzy-logic dead zone compensation takes center stage. This study embraces the intricacies of positioning control for an XY table, introducing advanced control strategies that counteract dead zone effects through adaptive control algorithms. Such an approach showcases the synergistic interplay between dynamic control and compensation, offering a comprehensive solution for enhanced motion precision. The aspiration for linear and seamless motion finds resonance in study [4], which introduces a groundbreaking linear piezomotor with minimized backward and nonlinear motion properties. Through ingenious engineering, an XY-direction decoupling displacement output is achieved, enabling a linear and continuous motion trajectory. Additionally, the incorporation of a flexure mechanism further elevates the motion's continuity, with friction enlisted as a crucial non-switching force within the dynamic equations. In the realm of load reduction and motion optimization, the CoreXY mechanism emerges as a pivotal player in study [5]. The study addresses the challenges associated with moving loads, where the elasticity of belt transmission introduces errors during high-speed motion along defined trajectories. The implementation of the CoreXY mechanism showcases its potential to mitigate these errors, enhancing system efficiency and performance. Building upon the CoreXY framework, study [6] offers a comprehensive exploration of kinematic and dynamic modeling. Through the lens of a one-belt-driven mechanism akin to CoreXY, the study employs Lagrange equations to dissect dynamic behaviors. Notably, the consideration of friction as a nonlinear model enriches the understanding of the system's intricate dynamics, albeit without specifying the role of friction at each pulley. A crucial realm of application emerges in 3D printer design, where the choice of print head positioning mechanism carries profound implications. Study [7] underscores the significance of this choice, delineating its far-reaching influence on manufacturing accuracy, speed, workspace characteristics, and overall cost. Through the innovative CoreH-bot, a harmonious blend of CoreXY and H-bot mechanisms, the study showcases the role of kinematic and dynamic modeling in optimizing precision through the integration of low-friction

bearings. Furthermore, study [8] sheds light on the intricacies of modeling robotic systems with closed-circuit belt-pulley transmissions. The study unveils the complexities of belt-pulley network friction, encompassing factors such as belt tension, pulley wrap angles, and the number of pulleys. Employing multi-friction models for pulleys, the research navigates the multifaceted interplay of frictional forces, further expanding the realm of dynamic modeling. Amidst this vibrant landscape, study [9] presents an exploration into a hollow-type XY piezoelectric positioning platform, unveiling a three-stage flexible lever amplification. This innovative platform design introduces a novel approach to motion amplification, with careful consideration of flexible mechanisms and piezoelectric properties. Such a study contributes to the rich tapestry of precision engineering, adding a layer of complexity and adaptability to motion systems.

Friction presents a significant challenge for control system design in many mechanical systems with contacting surfaces [10]. Both static and kinetic friction forces exist, and their inherent nonlinearities make precise mathematical modeling difficult [11]. The transition between these states and the point of movement initiation or cessation remains unclear. Due to these uncertainties, researchers often treat friction as a disturbance during control design. They then employ estimators, like state observers, to approximate its effects [12]. For instance, some researchers designed an observer to estimate dry friction effects on an inverted pendulum system, enabling control through state feedback [13], [14]. The constant switch between static and kinetic friction creates a cycle of motion and stoppages, known as stick-slip. This phenomenon can negatively impact control in systems with significant surface interaction. A switching model with feedback control is a viable approach for stick-slip prone systems, particularly those involving dry friction, such as brakes, servo systems, and drilling equipment [15]. For example, stick-slip is crucial in oil and gas drilling, where unpredictable environments and nonlinear friction forces lead to nonlinear equipment behavior [16]. Friction modeling needs to capture these switching dynamics effectively. The Stribeck model is a popular choice, providing insights into friction as a function of velocity [17]. However, friction in both static and kinetic states causes energy losses and increases actuator power demands for control. When the system is at rest, the actuator force must exceed static friction to initiate motion. This creates a dead zone where the system remains stationary regardless of the applied force. This dead zone can be symmetrical [18] or asymmetrical [19], [20].

1.2 Contributions of the research

As observed in the literature review, the CoreXY system, being a multi-body dynamic system, poses a complex and challenging modeling task. Some of the modeling challenges for this system include:

- The mechanism comprises various dynamic components exhibiting different motions, necessitating a thorough consideration of the interactions among the mechanism's components on the manipulator.
- Each actuator component of the system makes individual contact with the ground, and their dry friction with their supports opposes the system's actuation forces.
- The presence of dry friction between the system components and the ground leads to the creation of a multi-dimensional dead zone for manipulator motion, which can vary depending on the direction of motion of each mechanism component and the tensions in the belts.
- The friction of each mechanism's moving component can be of a static or kinetic nature resulting in the stick-slip phenomenon, requiring the calculation of different forces and torques in each case, necessitating the use of a switchable model.
- When using time-integration methods, it is necessary to check the dead zone conditions at each time step to determine whether the system is capable of motion or not.

This research significantly extends the existing body of knowledge on CoreXY mechanisms by introducing a dynamic modeling approach that incorporates the frictional states of the mechanism's constituent elements. Furthermore, the study explores the dead zone behavior, investigating its relationship with the tension forces influencing voltage inputs and torques. These unique contributions mentioned below yield a deeper insight into the intricate interactions within the CoreXY mechanism, providing key insights for optimizing its operational performance and enhancing control strategies.

- The entire mechanism is modeled as a 2-DoF dynamic system, and the dynamic equations, represented in matrix form, depict all the effects of the system's constituent components on the motion of the manipulator.
- All dry frictions present in various components of the system, which resist the motion of the manipulator, are stored in a vector denoted as b .

- Based on the velocity of each mechanism component at any given moment, it is determined whether its dry friction is of the static or kinetic type, thus calculating the dead zone interval based on the stationary components.
- By utilizing the two-step discrete Adams-Bashforth time-integration method, which is an explicit time scheme, the dynamic equations of the system are discretized, and the manipulator's acceleration is integrated to calculate velocity and position, considering the dead zone effects at the onset of motion.
- The relationship between the tensions in the belts and the multi-dimensional dead zone created is thoroughly analyzed and examined.

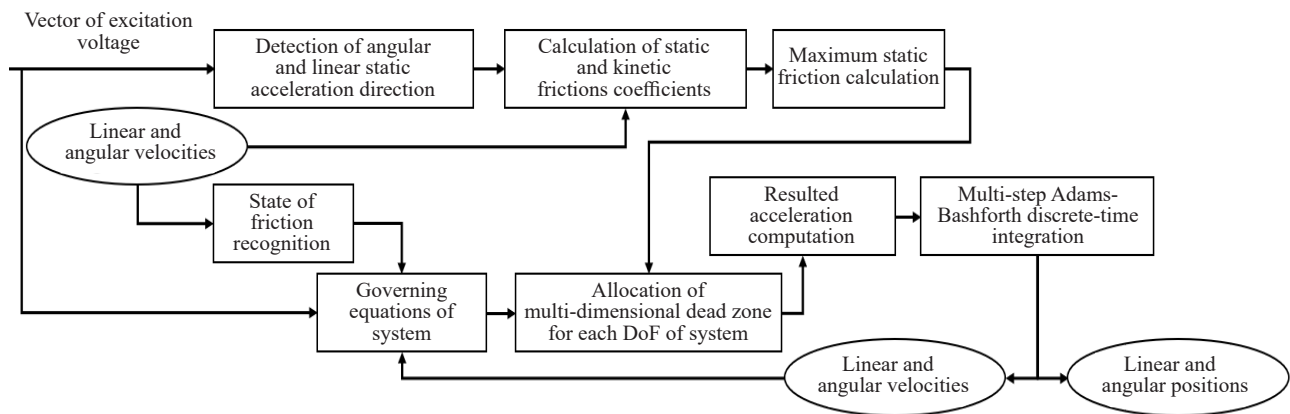


Figure 1. A comprehensive overview of the numerical simulation algorithm for the CoreXY mechanism, encompassing all stages, including friction computation and manipulator acceleration calculation, while considering multi-dimensional dead zone effects

Figure 1 illustrates the algorithm employed for the numerical simulation of the dynamic behavior of the CoreXY system, accounting for the non-linear effects of friction and the dead zone created within the dynamic equations.

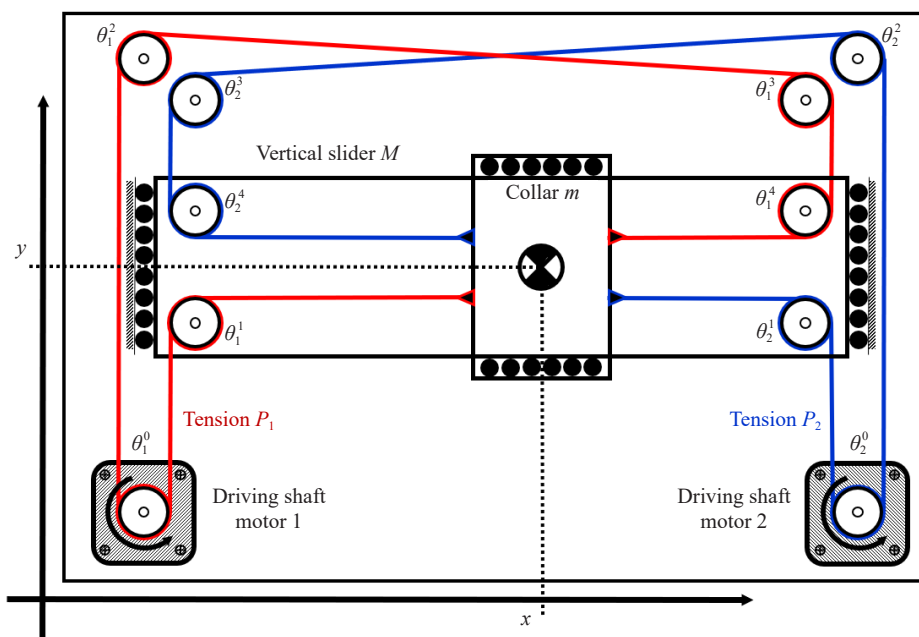


Figure 2. The CoreXY mechanism encompasses sliders, pulleys, actuator motors, and two motion transmission belts

2. CoreXY mechanism kinematics and dynamics

The CoreXY mechanism is a Cartesian mechanism that utilizes two motors and a set of pulleys to precisely determine the position of a collar on the XY plane. Figure 2 illustrates the CoreXY mechanism, which comprises two motors, eight torque transmission pulleys, two belts in red and blue colors, and two visible sliders with masses of m and M . By applying effective torque through each motor, forces are transmitted via the belts to the sliders, resulting in the movement of the collar within the XY plane.

2.1 CoreXY motion analysis and coupled kinematics determination

In this section, the kinematic relationships of the CoreXY mechanism will be derived. The kinematic equations encompass the interplay between the velocities and accelerations of the collar with the velocities and accelerations of the motors and pulleys. Drawing insights from Figure 2, the pulley velocities based on the collar's motion velocities in the XY plane can be expressed using Eqs. (1)-(10). In these equations, $\dot{\theta}$ represents the pulley velocities, \dot{x} and \dot{y} denote the linear velocities of the collar in the XY plane, and r signifies the radius of each pulley; for all the pulleys, the radius is the same.

$$\dot{\theta}_1^0 = \frac{\dot{x} + \dot{y}}{r} \quad (1)$$

$$\dot{\theta}_1^1 = -\frac{\dot{x}}{r} \quad (2)$$

$$\dot{\theta}_1^2 = \frac{\dot{x} + \dot{y}}{r} \quad (3)$$

$$\dot{\theta}_1^3 = \frac{\dot{x} + \dot{y}}{r} \quad (4)$$

$$\dot{\theta}_1^4 = \frac{\dot{x}}{r} \quad (5)$$

$$\dot{\theta}_2^0 = \frac{\dot{x} - \dot{y}}{r} \quad (6)$$

$$\dot{\theta}_2^1 = -\frac{\dot{x}}{r} \quad (7)$$

$$\dot{\theta}_2^2 = \frac{\dot{x} - \dot{y}}{r} \quad (8)$$

$$\dot{\theta}_2^3 = \frac{\dot{x} - \dot{y}}{r} \quad (9)$$

$$\dot{\theta}_2^4 = \frac{\dot{x}}{r} \quad (10)$$

Continuing, it is possible to ascertain the linear velocity of the collar in terms of the angular velocities of the two

motors, denoted respectively by $\dot{\theta}_1^0$ and $\dot{\theta}_2^0$. As evident from Eqs. (11)-(12), the collar's velocity in the x direction is a direct summation of the motor velocities, while its velocity in the y direction is a consequence of the difference between the motor velocities.

$$\dot{x} = \frac{r(\dot{\theta}_1^0 + \dot{\theta}_2^0)}{2} \quad (11)$$

$$\dot{y} = \frac{r(\dot{\theta}_1^0 - \dot{\theta}_2^0)}{2} \quad (12)$$

Taking into account Eqs. (1) and (6), it becomes possible to deduce the relationships between the accelerations of the motors and the linear accelerations of the collar, as expressed in Eqs. (13) and (14).

$$\dot{\omega}_1 = \frac{\ddot{x} + \ddot{y}}{r} \quad (13)$$

$$\dot{\omega}_2 = \frac{\ddot{x} - \ddot{y}}{r} \quad (14)$$

Remark 1 (Motion of belt and pulleys without relative slipping)

This paper disregards the slippage of belts around pulleys, which can occur due to sudden changes in pulley rotation speed. Despite this phenomenon, kinematic relationships have been derived.

Remark 2 (Negligible weight and axial flexibility of new-technology belts)

Nowadays, the technology used in manufacturing belts has reached a point where the material strength is so high that their elongation is at the micro level. This allows for disregarding the longitudinal elongation property with a high degree of precision. These modern belts, despite being thin and lightweight, possess significant strength, and the differential weight of their components can also be overlooked.

2.2 CoreXY kinetic analysis and dynamics

In this section, considering the motor torques as inputs to the system dynamics, the resulting accelerations within the system components will be computed. To achieve this, it is essential to depict the forces and torques exerted by each of the system elements, including the motors, pulleys, belts, and sliders, on a free-body diagram of the system, as depicted in Figure 3. Subsequently, dynamic equations can be derived. As seen in Figure 3, the effective torques of the motors are denoted by τ^E , belt tension forces by T , and the torques arising from friction are represented by τ_1 for the red belt components and τ_2 for the blue belt components. Additionally, the vertical surface forces, dependent on the belt tension forces, are shown as N . The motion of the sliders also gives rise to frictional forces, denoted as f_x and f_y in the x and y directions, respectively.

It's assumed that the tension force in the red and blue belts before the application of torques and motion is denoted by P_1 and P_2 , respectively. Furthermore, in this paper, it is assumed that the belts do not experience any slack relative to the pulleys and exhibit a rolling motion. Following the application of a positive torque to the left-side motor, the tension forces on the left and right sides of the motor increase and decrease respectively, a change denoted by ΔP_1 . Consequently, the aforementioned tension forces can be approximated using Eqs. (15)-(16). In these equations, the magnitude of ΔP_1 is unspecified, rendering the calculation of individual tension forces unfeasible. However, their sum can be approximated as $2P_1$, as indicated by Eq. (17).

$$T_1^0 = P_1 - \Delta P_1 \quad (15)$$

$$T_2^0 = P_1 + \Delta P_1 \quad (16)$$

$$T_1^0 + T_2^0 = 2P_1 \quad (17)$$

Consequently, assuming that the vertical surface forces for each of the pulleys are applied as point forces to the center of the belt coiled around the pulley, the vertical surface force for each pulley can be computed by vector summing the tension forces on the left and right sides of the pulley. Therefore, the vertical surface force for the left and right motors will be $N_1^0 = 2P_1$ and $N_2^0 = 2P_2$, respectively. Additionally, for the other pulleys, considering that the angle between the left and right tension forces for each is nearly 90 degrees, the vertical surface force for the pulleys in contact with the red and blue belts can be approximated as $\sqrt{2}P_1$ and $\sqrt{2}P_2$, respectively. Furthermore, for the sliders, it can be assumed that vertical surface forces are equivalent to the weight placed upon the rails. Hence, the vertical surface force on the horizontal rail is $N_x = mg$, while the vertical surface force on the vertical rail is $N_y = (M + m)g$.

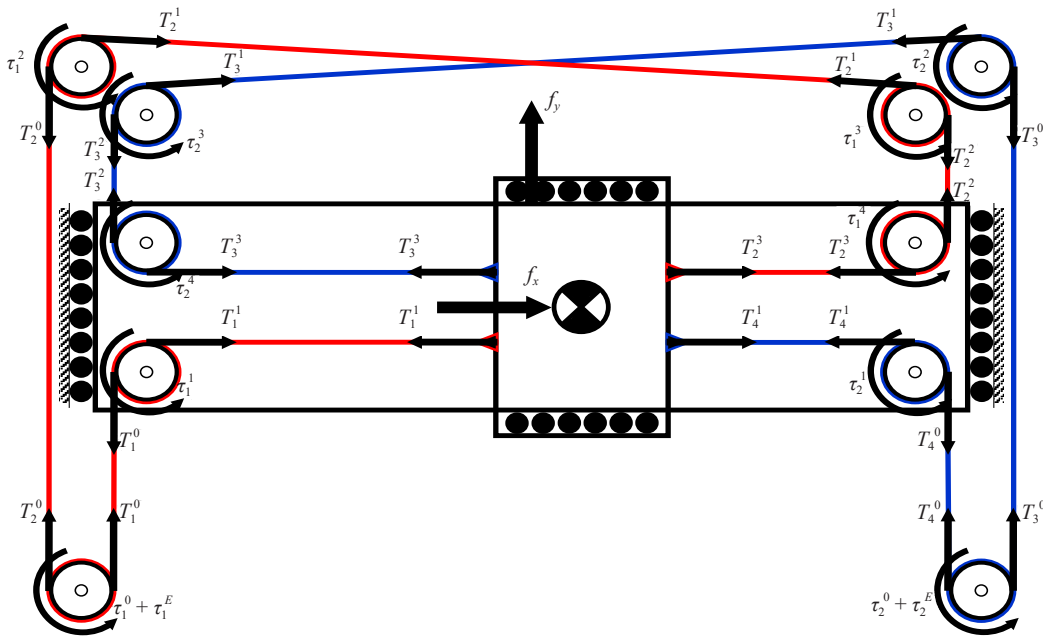


Figure 3. The free-body diagram of the CoreXY mechanism components, illustrating the applied forces and torques on each element of the system

2.3 Extraction of coupled equations of motion of the CoreXY mechanism

Continuing, considering the forces and torques applied to each element of the CoreXY mechanism, the dynamic equations of the system will be derived. In accordance with Newton's second law, Eqs. (18)-(19) represent the dynamic equations for the motors' pulleys on the left and right sides. In these equations, the torques applied to the motors, after subtracting the torques resulting from dry friction denoted as τ , induce angular accelerations $\dot{\omega}$ to each of the motors. These accelerations arise from the rotational inertia J possessed by the motors.

$$+T_1^0 r - T_2^0 r + \tau_1^0 + \tau_1^E = J\dot{\omega}_1 \quad (18)$$

$$+T_3^0 r - T_4^0 r + \tau_2^0 + \tau_2^E = J\dot{\omega}_2 \quad (19)$$

The closest pulleys to each of the motors are the pulleys θ_1^1 and θ_2^1 , and their dynamic equations are presented in Eqs. (20)-(21).

$$+T_1^0 r - T_1^1 r + \tau_1^1 = J' \frac{-\ddot{x}}{r} \quad (20)$$

$$+T_4^1 r - T_4^0 r + \tau_2^1 = J' \frac{-\ddot{x}}{r} \quad (21)$$

where J' represents the rotational inertia of each of the pulleys and the pulley's angular acceleration is determined by the system's kinematics, given by $\frac{-\ddot{x}}{r}$. The four pulleys situated atop the sliders are positioned on the ground and share the same velocity and acceleration as their corresponding motors. As a result, the dynamic equations for the four pulleys atop the sliders can be derived as shown in Eqs. (22)-(25).

$$+T_2^0 r - T_2^1 r + \tau_1^2 = J' \dot{\omega}_1 \quad (22)$$

$$+T_3^1 r - T_3^0 r + \tau_2^2 = J' \dot{\omega}_2 \quad (23)$$

$$+T_2^1 r - T_2^2 r + \tau_1^3 = J' \dot{\omega}_1 \quad (24)$$

$$+T_3^2 r - T_3^1 r + \tau_2^3 = J' \dot{\omega}_2 \quad (25)$$

The dynamic equations concerning the pulleys θ_1^4 and θ_2^4 can similarly be formulated as Eqs. (26)-(27). As observed, the angular acceleration of these two pulleys exhibits a direct relationship with the positive \ddot{x} direction.

$$+T_2^2 r - T_2^3 r + \tau_1^4 = J' \frac{+\ddot{x}}{r} \quad (26)$$

$$+T_3^3 r - T_3^2 r + \tau_2^4 = J' \frac{+\ddot{x}}{r} \quad (27)$$

Taking into consideration the tension forces applied to each of the sliders as well as the frictional forces on the rails, the dynamic equations for the sliders can also be expressed as depicted in Eqs. (28)-(29).

$$+T_2^3 + T_4^1 - T_3^3 - T_1^1 + f_x = m\ddot{x} \quad (28)$$

$$+T_2^2 + T_3^2 - T_1^0 - T_4^0 + f_y = (M + m)\ddot{y} \quad (29)$$

wherein f_x and f_y respectively represent the frictional forces applied to the collar and the vertical slider.

2.4 Matching and adapting permanent magnet DC motor equations into the CoreXY dynamics

In this section, considering the dynamic equations of the permanent magnet DC motors employed within the mechanism, the generated motor torques will be computed. As noted in study [21], it is possible, with approximation, to formulate the dynamic equations of permanent magnet DC motors as depicted in Eqs. (30)-(33).

$$\tau_1^E = K_t i_1 \quad (30)$$

$$\tau_2^E = K_t i_2 \quad (31)$$

$$i_1 = -\frac{K_e}{R} \omega_1 + \frac{1}{R} v_1 \quad (32)$$

$$i_2 = -\frac{K_e}{R} \omega_2 + \frac{1}{R} v_2 \quad (33)$$

where K_t denotes the torque coefficient, i signifies the current intensity generated in the motor armature, K_e represents the back EMF coefficient, R stands for motor resistance, and v symbolizes the input voltage of each of the permanent magnet DC motors. Considering the voltages v_1 and v_2 as inputs to the system dynamics, the dynamic equations of the CoreXY mechanism can be expressed as Eq. (34).

From this point onward, for better visualization of the dynamic equations and to establish a connection between all components of the system with the manipulator, the equations will be presented in the matrix form. As seen in Eq. (34), by utilizing the system's kinematic relationships, the relationship between the input voltages and the manipulator's accelerations has been derived. Essentially, this relationship encompasses all interactions present in this 2-DoF system.

$$\mathcal{M}\ddot{\underline{x}} = \mathcal{C}\dot{\underline{x}} + \underline{b}(\dot{\underline{x}}, P_1, P_2, \mu_k) + \mathcal{B}\underline{v} \quad (34)$$

wherein the vector \underline{x} comprises the position variables of the collar, and the vector \underline{v} encompasses the voltage inputs of each of the motors, as defined in Eq. (35).

$$\underline{x} \triangleq \begin{bmatrix} X \\ y \end{bmatrix}; \quad \underline{v} \triangleq \begin{bmatrix} v_1 \\ v_2 \end{bmatrix} \quad (35)$$

In Eq. (34), the matrix \mathcal{M} represents the system's inertia matrix, which is computed as a diagonal matrix from the relationship given by Eq. (36).

$$\mathcal{M} = \begin{bmatrix} mr + \frac{8J'}{r} + \frac{2J}{r} & 0 \\ 0 & (M+m)r + \frac{4J'}{r} + \frac{2J}{r} \end{bmatrix} \quad (36)$$

Furthermore, the matrices \mathcal{C} and \mathcal{B} , representing the velocity coefficients matrix and the input coefficients matrix, respectively are computed using Eqs. (37) and (38).

$$\mathcal{C} = \begin{bmatrix} \frac{-2K_t K_e}{rR} & 0 \\ 0 & \frac{-2K_t K_e}{rR} \end{bmatrix} \quad (37)$$

$$\mathcal{B} = \frac{K_t}{R} \begin{bmatrix} +1 & +1 \\ +1 & -1 \end{bmatrix} \quad (38)$$

With reference to Eq. (37), it can be observed that the acceleration in the x direction is dependent on $v_1 + v_2$, while the acceleration in the y direction is contingent on $v_1 - v_2$.

$$\underline{b}(\underline{\dot{x}}, P_1, P_2, \mu) = \begin{bmatrix} +\tau_1^0 + \tau_1^1 + \tau_1^2 + \tau_1^3 + \tau_1^4 + \tau_2^0 + \tau_2^1 + \tau_2^2 + \tau_2^3 + \tau_2^4 + f_x r \\ +\tau_1^0 + \tau_1^2 + \tau_1^3 - \tau_2^0 - \tau_2^2 - \tau_2^3 + f_y r \end{bmatrix} \quad (39)$$

The coefficients of friction opposing the motion of system components are also stored in the vector \underline{b} , which is computed using Eq. (39).

2.5 Application of Adams-Bashforth discretization method to CoreXY dynamics

To discretize the dynamic equations of the system, the Adams-Bashforth method can be employed. Assuming that the variable ϕ , resulting from the integration of its derivative $\dot{\phi}$, is under consideration, and $\phi(k)$ can be computed in terms of $\dot{\phi}(k-1)$ using Eq. (40) [10].

$$\phi(k) = \phi(k-1) + \frac{3T}{2}\dot{\phi}(k-1) - \frac{T}{2}\dot{\phi}(k-2) \quad (40)$$

Consequently, the dynamic equations of the system can be discretized by introducing state variables as defined in Eq. (41), leading to the discretized equations as shown in Eqs. (42)-(45).

$$\underline{x}_1 = \underline{x}; \quad \underline{x}_2 = \underline{\dot{x}} \quad (41)$$

$$\underline{\dot{x}}_1 = \underline{x}_2 \quad (42)$$

$$\underline{\dot{x}}_2 = \mathcal{M}^{-1} [\mathcal{C}\underline{\dot{x}} + \underline{b}(\underline{\dot{x}}, P_1, P_2, \mu) + \underline{B}\underline{v}] \quad (43)$$

$$\underline{x}_1(k) = \underline{x}_1(k-1) + \frac{3T}{2}\underline{x}_2(k-1) - \frac{T}{2}\underline{x}_2(k-2) \quad (44)$$

$$\begin{aligned} \underline{x}_2(k) &= \underline{x}_2(k-1) + \frac{3T}{2}\underline{\dot{x}}_2(k-1) - \frac{T}{2}\underline{\dot{x}}_2(k-2) \\ &= \underline{x}_2(k-1) + \frac{3T}{2}\mathcal{M}^{-1} [\mathcal{C}\underline{x}_2(k-1) + \underline{b}[\underline{x}_2(k-1), P_1, P_2, \mu] + \underline{B}\underline{v}(k-1)] \\ &\quad - \frac{T}{2}\underline{\dot{x}}_2(k-2) \end{aligned} \quad (45)$$

3. Static and kinetic friction modes recognition algorithm

Taking into account the nature of friction present between contacting surfaces, it is necessary to examine various friction scenarios. In general, two modes of friction can be expressed, depending on the body's motion speed; kinetic or static. Assuming that the linear or angular velocity of a body is represented by $\dot{\phi}_i$ and its acceleration by $\ddot{\phi}_i$, the force or torque resulting from friction applied to the body can be computed and incorporated into the matrix $\underline{b}(\underline{\dot{x}}, P_1, P_2, \mu)$.

3.1 Kinetic mode recognition logic

In the first scenario, where the linear or angular velocity of the body, denoted as $\dot{\phi}(k-1) \neq 0$, the friction applied to the body is kinetic. Its magnitude is calculated using Eq. (46).

$$\mathcal{F}_{ik}(k-1) = -\mu_{ik} N_i \operatorname{sgn}[\dot{\phi}_i(k-1)] \quad (46)$$

in which, $\mathcal{F}_{ik}(k-1)$ represents the force or torque resulting from kinetic friction applied to the body, directed opposite to the motion of the body. μ_{ik} denotes the coefficient of kinetic friction for the body and N_i corresponds to the vertical surface force applied to the body.

Remark 3 (The impact of tension forces on the magnitude of frictional forces and torques)

As seen in Eq. (46), the normal force N_i has appeared, the values of which can be calculated for each of the mechanism pulleys, as well as in the x (horizontal) and y (vertical) directions for the sliders, as explained in Section 2.2. It is evident that since the normal forces depend on the tension forces P_1 and P_2 , therefore, the frictional values will also be proportional to the tension forces. Thus, with an increase in the magnitude of the tension forces, the frictional values also increase, leading to an increase in the mechanical resistance against motion.

3.2 Static mode recognition logic

In the second scenario, the body is stationary and non-rotating, meaning its linear or angular velocity is $\dot{\phi}(k-1) = 0$. In this case, the force or torque resulting from static friction applied to the body is computed using Eq. (47). Wherein, $\mathcal{F}_{is}(k-1)$ represents the force or torque resulting from static friction applied to the body, directed opposite to the direction in which the body would tend to move, i.e., the direction indicated by the body's acceleration. μ_{is} also signifies the coefficient of static friction for the body.

$$\mathcal{F}_{is}(k-1) = -\mu_{is} N_i \operatorname{sgn}[\ddot{\phi}_i(k-1)] \quad (47)$$

As observed, the velocities of the pulleys were computed in terms of the linear velocity of the collar in the XY plane during the kinetic analysis. In this section, it is necessary to determine the accelerations of the system components. Since the accelerations of the collar variables, namely $\ddot{x}(k-1)$ and $\ddot{y}(k-1)$, are dependent on the time-based inputs at time step $k-1$, it is not possible to calculate the accelerations before applying the inputs. However, their signs can be determined when their velocities are zero, and these signs can be used in Eq. (47). For this purpose, considering Eq. (43), which is utilized for calculating accelerations at time step $k-1$, the signs of the accelerations of the collar variables can be computed using Eqs. (48) and (49).

$$\dot{x}(k-1) = 0 : \operatorname{sgn}[\ddot{x}(k-1)] = \operatorname{sgn}[\mathbf{B}\underline{v}(k-1)]_1 \quad (48)$$

$$\dot{y}(k-1) = 0 : \operatorname{sgn}[\ddot{y}(k-1)] = \operatorname{sgn}[\mathbf{B}\underline{v}(k-1)]_2 \quad (49)$$

where $\operatorname{sgn}[\mathbf{B}\underline{v}(k-1)]_1$ and $\operatorname{sgn}[\mathbf{B}\underline{v}(k-1)]_2$ represent the signs of the first and second rows of the matrix $\mathbf{B}\underline{v}(k-1)$, respectively.

3.3 Mechanism coupled dead zone analysis and determination

In the scenario where the body's velocity is zero and external forces or torques are applied, two cases can occur. The first case is when the magnitude of the applied force or torque is smaller than the maximum static friction, resulting in the force or torque falling within the dead zone range. Consequently, the body will experience zero acceleration in that direction. The second case is when the magnitude of the applied force or torque is sufficiently large to overcome static friction, leading to acceleration in the body. In the second case, the body's acceleration is determined by the

difference between the applied force or torque and the static friction. Eq. (50) represents the values of applied forces in the x and y directions, denoted respectively as $v_x(k-1)$ and $v_y(k-1)$.

$$\begin{bmatrix} v_x(k-1) \\ v_y(k-1) \end{bmatrix} = \mathbf{B}\underline{v}(k-1) \quad (50)$$

Furthermore, the values of frictional forces and torques are stored in the vector $\underline{b}_s(k-1)$, accounting for the maximum static friction. This vector is computed using Eq. (51).

$$\begin{aligned} \underline{b}_s(k-1) &= \begin{bmatrix} b_{s1}(k-1) \\ b_{s2}(k-1) \end{bmatrix} \\ &= \begin{bmatrix} +\tau_{1s}^0 + \tau_{1s}^1 + \tau_{1s}^2 + \tau_{1s}^3 + \tau_{1s}^4 + \tau_{2s}^0 + \tau_{2s}^1 + \tau_{2s}^2 + \tau_{2s}^3 + \tau_{2s}^4 + f_{xs}r \\ +\tau_{1s}^0 + \tau_{1s}^2 + \tau_{1s}^3 - \tau_{2s}^0 - \tau_{2s}^2 - \tau_{2s}^3 + f_{ys}r \end{bmatrix} \end{aligned} \quad (51)$$

where the values on the right-hand side of the equation can be computed using Eq. (47).

3.3.1 Inside partition of the coupled dead zone of dynamic equations

As evident from Eqs. (52)-(53), in this scenario, the acceleration of the body in the corresponding direction will be zero, assuming that the magnitude of the input stimulus is insufficient to initiate motion and the body has entered the dead zone.

$$\dot{x}(k-1) = 0, \quad |v_x(k-1)| \leq |b_{s1}(k-1)| \Rightarrow \ddot{x}(k-1) = 0 \quad (52)$$

$$\dot{y}(k-1) = 0, \quad |v_y(k-1)| \leq |b_{s2}(k-1)| \Rightarrow \ddot{y}(k-1) = 0 \quad (53)$$

3.3.2 Outside partition of the coupled dead zone of dynamic equations

In this scenario, it is assumed that the magnitude of the input stimulus to the stationary body can overcome static friction and induce acceleration in the corresponding direction. In this case, the acceleration of the body can be calculated using Eqs. (54)-(56).

$$\ddot{\underline{x}} = \mathcal{M}^{-1} \left[\mathbf{C}\dot{\underline{x}} + \underline{b}(\dot{\underline{x}}, P_1, P_2, \mu_s) + \mathbf{B}\underline{v} \right] \quad (54)$$

$$\dot{x}(k-1) = 0, \quad |v_x(k-1)| > |b_{s1}(k-1)| \Rightarrow \ddot{x}(k-1) \neq 0 \quad (55)$$

$$\dot{y}(k-1) = 0, \quad |v_y(k-1)| > |b_{s2}(k-1)| \Rightarrow \ddot{y}(k-1) \neq 0 \quad (56)$$

Furthermore, it is possible to compute the dead zone interval for the input voltage of the system. For this purpose, it is necessary to first calculate the inverse of matrix \mathbf{B} using Eq. (57), and then the dead zone interval for both x and y directions can be calculated using Eq. (58).

$$\mathbf{B}^{-1} = \frac{R}{2K_f} \begin{bmatrix} +1 & +1 \\ +1 & -1 \end{bmatrix} \quad (57)$$

$$\begin{bmatrix} v_{d1} \\ v_{d2} \end{bmatrix} = \mathbf{B}^{-1} \begin{bmatrix} v_x(k-1) \\ v_y(k-1) \end{bmatrix} = \mathbf{B}^{-1} \underline{\mathbf{b}}_s(k-1) \quad (58)$$

4. Analysis and discussion of numerical simulations

In this section, in order to better analyze the dynamic behavior of the CoreXY mechanism and its various aspects, the system is simulated using the parameters provided in Table 1. The simulation involves applying different voltage inputs to the two motors of the system and performing integration using the Adams-Bashforth method.

Table 1. Parameters employed in the simulation of the CoreXY mechanism along with explanations

Parameter	Description	Value	Parameter	Description	Value
T [sec]	Time step	0.001	μ_{1k}	Red belt kinetic friction coeff.	0.2
m [kg]	Collar mass	0.5	μ_{1s}	Red belt static friction coeff.	0.4
M [kg]	Vertical slider mass	1	μ_{2k}	Blue belt kinetic friction coeff.	0.2
J [kg · m ²]	Rotor inertia	0.001	μ_{2s}	Blue belt static friction coeff.	0.4
J' [kg · m ²]	Pulley inertia	0.0005	μ_{xk}	Horizontal rail kinetic friction coeff.	0.2
r [m]	Pulley radius	0.05	μ_{xs}	Horizontal rail static friction coeff.	0.4
R [Ω]	Resistance	0.9	μ_{yk}	Vertical rail kinetic friction coeff.	0.2
K_t [N · m/amp]	Torque coeff.	2	μ_{ys}	Vertical rail static friction coeff.	0.4
K_e [volt/rad/sec]	Back EMF coeff.	0.03	P_1, P_2 , [N]	Belt tensions	Variable

Firstly, by applying piecewise rectangular voltage inputs to the motors, the behavior of the mechanism is investigated. As depicted in Figure 4(a), the position of the collar in the XY plane is plotted in response to the applied piecewise rectangular inputs. Additionally, the torque values for each direction, denoted as v_x and v_y , are calculated using the mapping provided in Eq. (50). In Figure 4(a), the regions within the dead zone are calculated based on the values of the vector $\underline{\mathbf{b}}_s$ and are highlighted in the diagram. Figure 4(b) illustrates the voltage input values, applied torques, and dead zone regions due to the presence of friction. Furthermore, to gain a better understanding of the dynamic behavior of the mechanism, its position and velocity in the XY plane are plotted. As observed in Figure 4(b), the applied torque values fall outside the dead zone range, thus allowing the system to overcome friction and initiate motion.

In order to examine the impact of dead zones on the system behavior, the voltage inputs can be gradually increased over time to initiate the system's motion, as depicted in Figure 5(a). As observed in Figure 5(b), by setting the voltage input of the second motor to zero, the voltage input to the first motor has linearly increased, resulting in an escalation of applied torques in both directions. Since the torque in the x direction is directly related to the sum of voltages, and the torque in the y direction is related to the difference between voltages, both torques have increased with the rising voltage of the first motor. Upon exceeding the dead zone boundaries for both torque directions, the system has initiated motion in the corresponding direction.

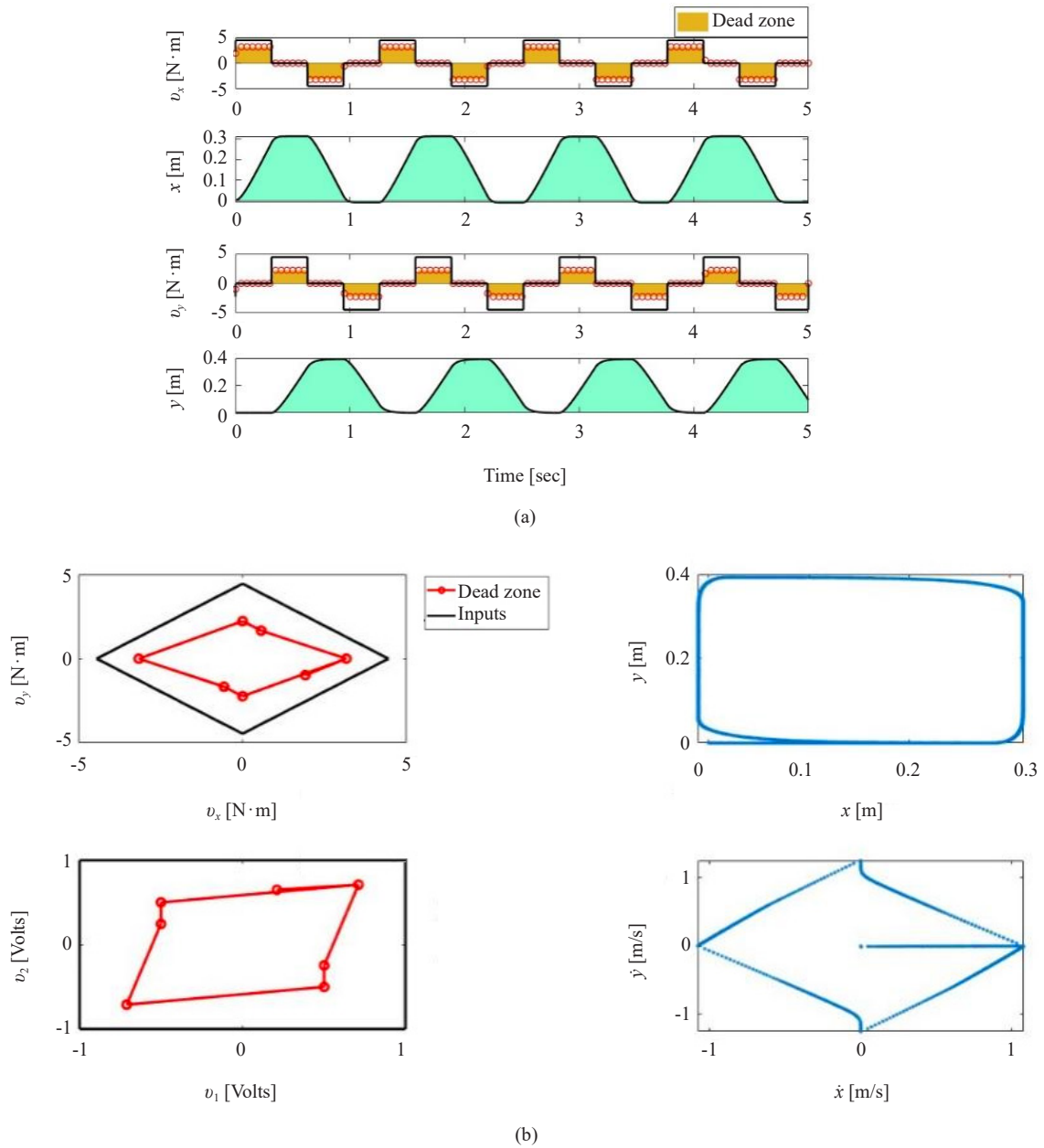


Figure 4. System response to piecewise rectangular stimulus input. (a) Generated torque values along with collar position variables in the XY plane and (b) dead zones related to voltage inputs and torques alongside voltage input and torque values, as well as collar position and velocity in the XY plane

Figure 6 represents the system's response to frequency analysis. In this method, the voltage inputs to the motors initiate motion within a constant amplitude circle, resulting in the generation of harmonic torques in both the x and y directions. As depicted in Figure 6(a), applying oscillatory voltages to the motors leads to the production of harmonic torques in the x and y directions, some of which may fall within the dead zone region. By introducing harmonic torques to the system, the harmonic behavior of the mechanism can also be observed in both the x and y directions. Figure 6(b) illustrates the produced torques along with the dead zone boundaries. By applying harmonic voltages, harmonic torques are generated that extend beyond the dead zone boundaries, inducing the motion of the mechanism in the XY plane. In Figure 6(b), the magnitude of the torques depends on the voltage amplitude of the motors, denoted as v_0 , and a larger amplitude results in a wider radius curve of the torque plot. Additionally, the size of the dead zone is influenced by the

tension forces P_1 and P_2 ; stronger tension forces lead to a broader dead zone range, which may intersect with the torque curve.

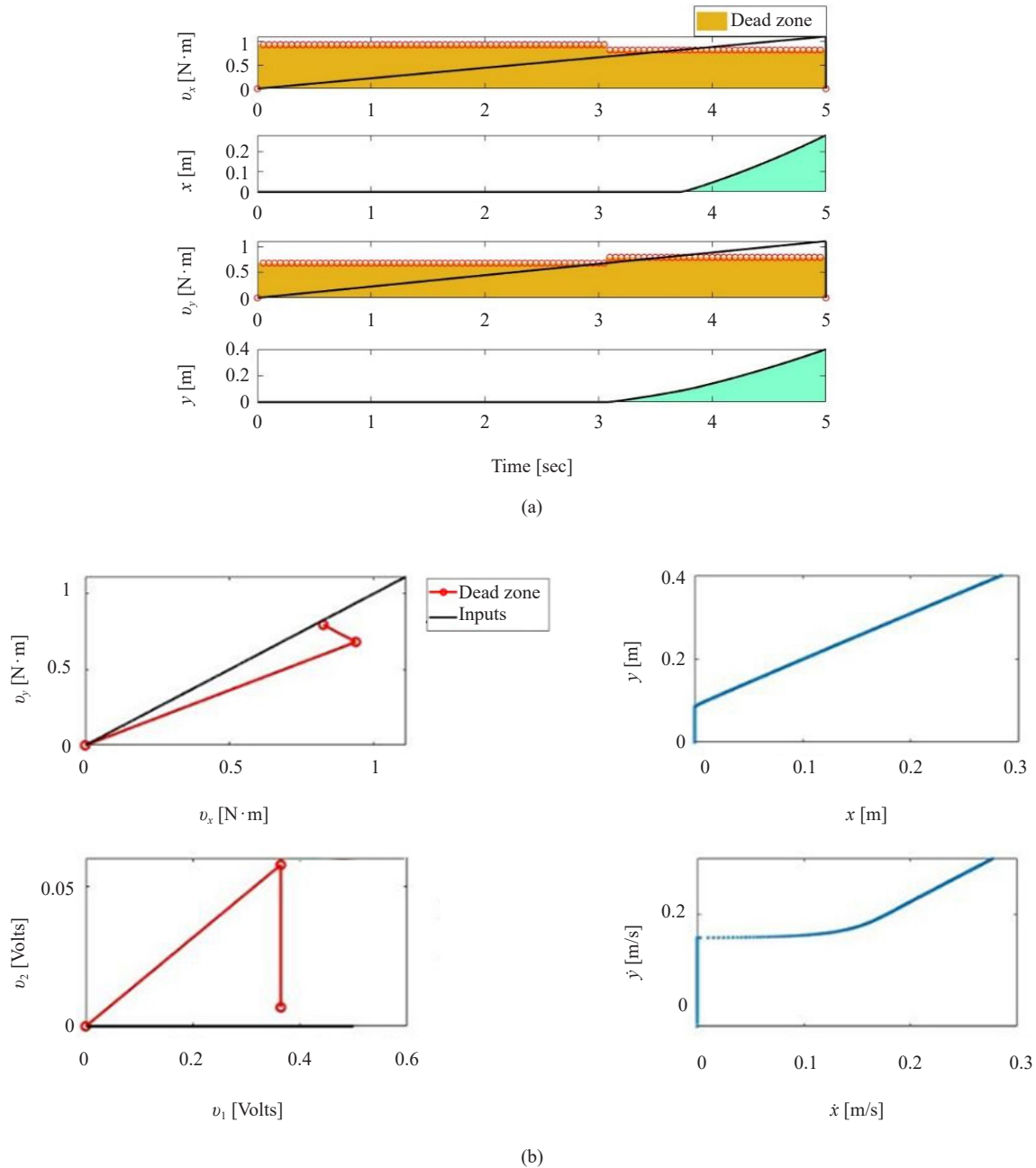


Figure 5. Effect of dead zones on system motion with increasing input. (a) Produced torque values along with dead zone regions and collar position in the XY plane. (b) Voltage input values for motors and corresponding torques in each direction, including dead zone values and collar's path of motion

Continuing the analysis, the input voltage amplitude is halved, and the tension forces are doubled. As observed in Figure 7(a), the torque curve with the dead zone range has intersected, causing the system to come to a halt in the x -direction and have a slight movement in the y -direction. Since the torque in the x -direction is entirely within the dead zone, there is no movement in the x -direction. However, in the y -direction, the curve has managed to exit the dead

zone slightly, resulting in movement only along the y -axis. By increasing the tension forces, as seen in Figure 7(b), the dead zone region expands, and both voltage inputs and generated torques are completely confined within the dead zone regions. Consequently, the mechanism is unable to accelerate and move in any direction.

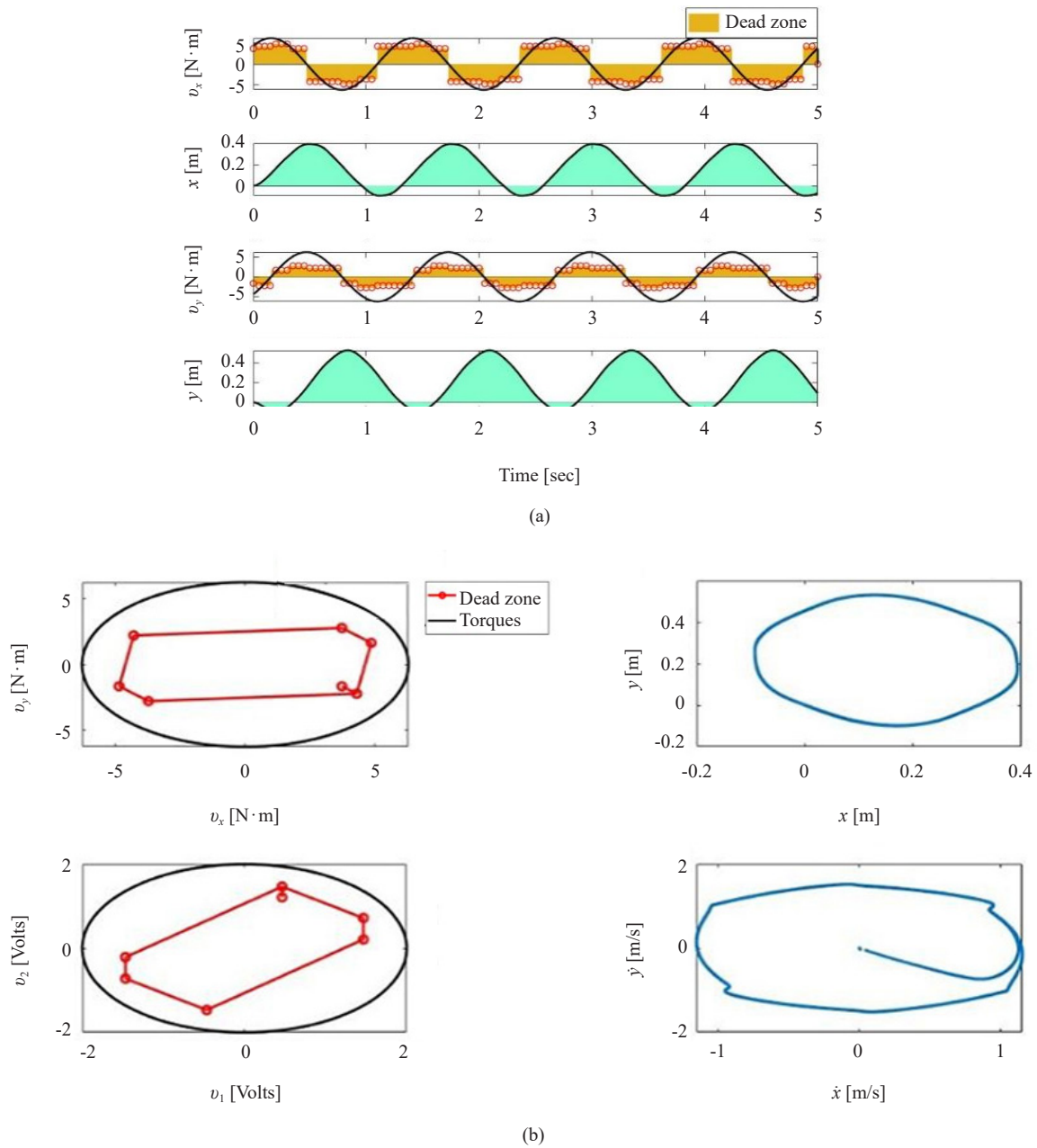


Figure 6. System response to frequency analysis. (a) Applied torque values in each direction and collar position variables in the XY plane. (b) Placement of motor voltages and generated torques outside the dead zone range, resulting in system motion in the XY plane for $P_1 = 1$ N, $P_2 = 1$ N, and $v_0 = 2$ Volts

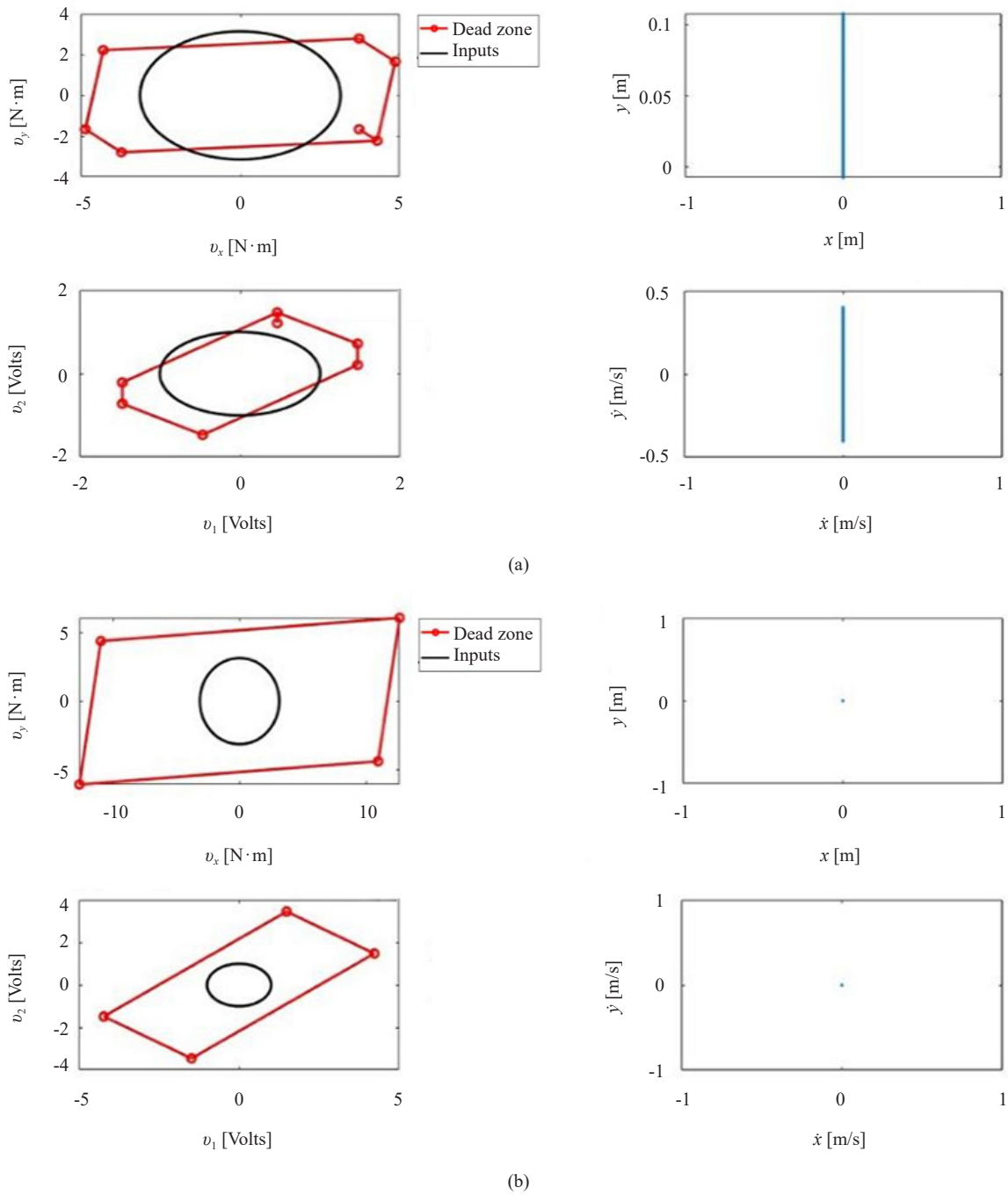


Figure 7. The intersection of inputs with dead zone range and disturbance in system movement for $P_1 = 2$ N and $P_2 = 2$ N, $v_0 = 1$ Volts. (b) Inputs within the dead zone range and no system movement for $P_1 = 3$ N and $P_2 = 3$ N, $v_0 = 1$ Volts

As mentioned, increasing the tension forces will result in a larger dead zone range. To examine the effects of tension forces on the dead zone, the results have been plotted by varying these forces proportionally using a coefficient denoted as α . First, while keeping the force P_2 at a constant value of 2 N, the force P_1 is increased as a coefficient of P_2 , i.e., $P_1 = \alpha P_2$, and the dead zone ranges are illustrated in Figure 8(a). With an increase in the coefficient α , it can be observed that the dead zone area also becomes larger asymmetrically and at an inclined angle. Conversely, by maintaining P_1 at 2 N and applying $P_2 = \alpha P_1$, the dead zone ranges are displayed in Figure 8(b), which have become larger in an inclined

manner opposite to the previous case.

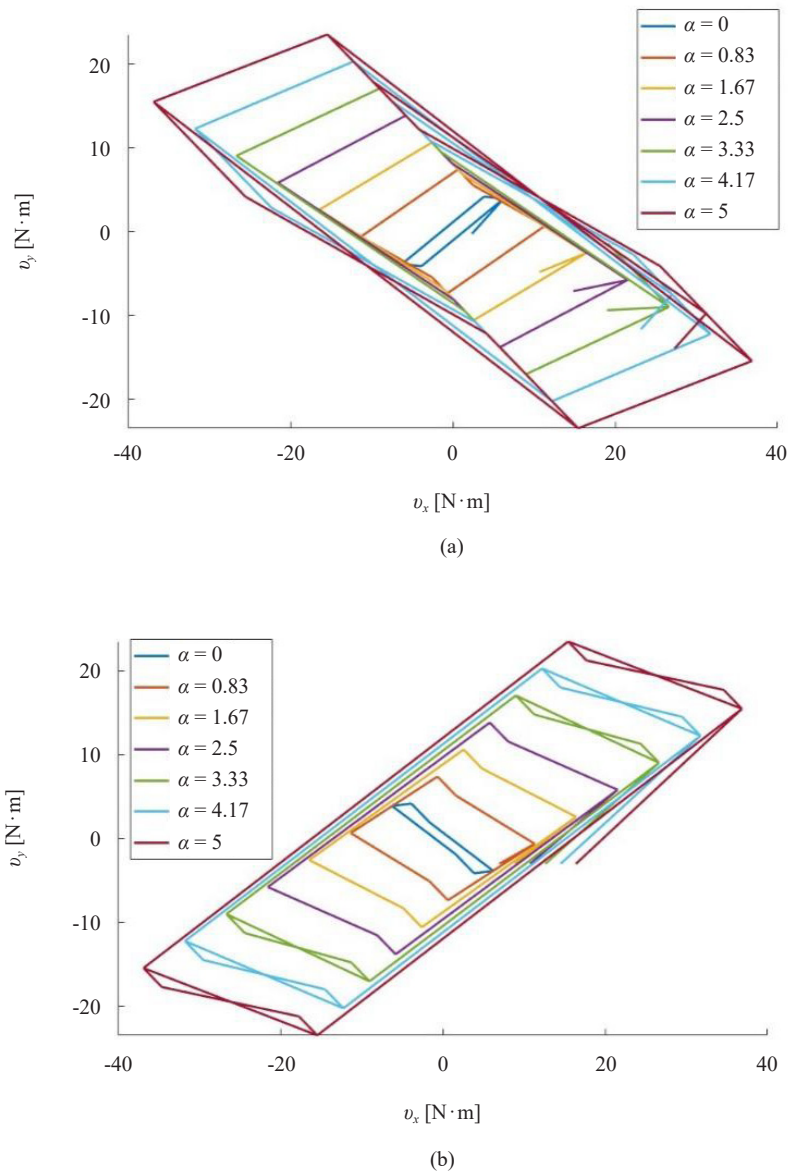


Figure 8. Dead zone region of torques as a function of tension forces. (a) Changes in the dead zone region for varying force P_1 , and (b) changes in the dead zone region for varying force P_2

Therefore, increasing each of the tension forces individually can expand the dead zone region in one direction. By simultaneously increasing both tension forces proportionally, such that $P_1 = P_2 = 2\alpha$, a symmetric expansion of the dead zone region can be observed in Figure 9.

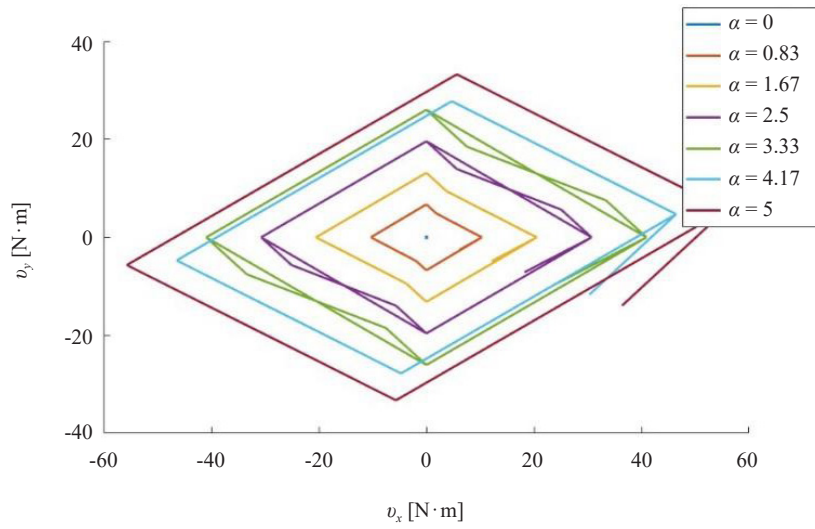


Figure 9. Variations in the dead zone region of torques with proportional and symmetric increases in tension forces

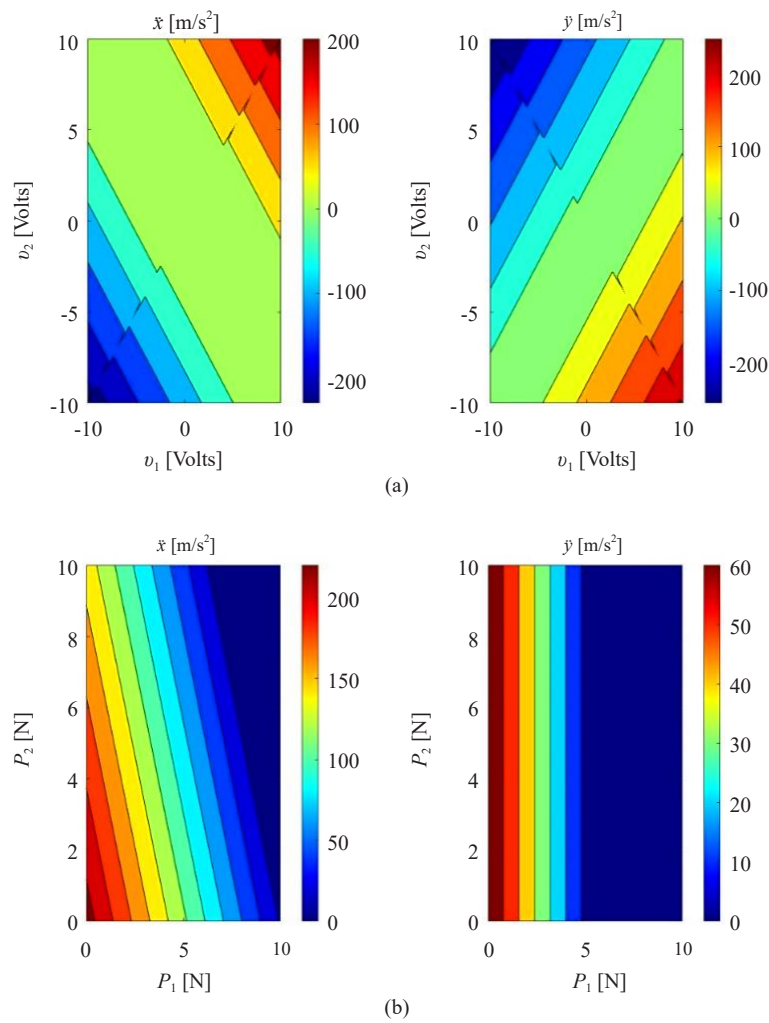


Figure 10. (a) dead zone region of accelerations for various motor voltages. (b) dead zone region of accelerations for different tension forces

Illustrative graphs in Figure 10 have been plotted to observe the dead zone during the mechanism's acceleration. In Figure 10, by assuming zero velocity in both the x and y directions, the system's acceleration, which induces motion, has been computed. In Figure 10(a), the acceleration of the collar in the x and y directions is depicted for various motor voltages. On the v_1v_2 plane, the region surrounding the line $v_1 + v_2 = 0$ indicates where the torque in the x direction falls within the dead zone. Likewise, the region around the line $v_1 - v_2 = 0$ signifies where the torque in the y direction falls within the dead zone. Moving away from these regions amplifies the magnitudes of the generated torques, enabling the system to accelerate beyond the dead zone. Figure 10(b) illustrates the values of collar acceleration for different tension forces. With an increase in tension forces, the dead zone area expands, leading to a reduction in the magnitude of the acceleration step until it reaches zero.

Therefore, due to the presence of frictional forces and torques in the mechanism, there will be a range in the input voltages where no acceleration will be generated when operating within that range. Consequently, when the mechanism is at rest, no motion will occur, and if the mechanism is in motion, its speed will be reduced until it comes to a stop. Taking into account the friction coefficients and different motion scenarios of the mechanism's components, it is essential to accurately calculate the dead zone range for both the initialization and motion control of the mechanism.

5. Conclusions

In conclusion, this study delved into the intricate realm of the CoreXY mechanism's kinematics and dynamics, with a specific focus on the nuanced motion of the collar plate. Throughout this exploration, the profound influence of friction on the system's dynamics took center stage, warranting meticulous integration into the equation derivation process. The discernible manifestations of friction, spanning static and kinetic domains, emerged as potential motivator for the emergence of dead zone regions within the operational scope of the system. By meticulously dissecting these dead zone regions, the paper casts a thorough illumination on their intricate characteristics, while simultaneously executing precise computations of friction across the myriad modes embedded within the system's components. Notably, the pivotal role played by tension forces within the belts surfaced as a pivotal factor, significantly contributing to the genesis of these dead zone areas. This intricate interplay was further dissected, revealing the extent to which tension forces intricately shape the mechanical dynamics of the system. Through a series of astute simulation endeavors, the interrelation between dead zones, tension forces, and the dynamic behaviors of the system was unveiled, presenting a vivid panorama of scenarios wherein actuator inputs nestled within or ventured beyond the confines of these dead zone territories. The culmination of these investigations yielded an invaluable repository of derived equations, encapsulating the multifaceted nature of friction-exposed systems, thus providing an encompassing perspective for the broader domain of modeling and analysis. In summary, the main conclusions of this paper will be listed as follows:

- Friction, both static and kinetic, significantly influences the system's dynamics. Its effects were meticulously integrated into the equation derivation to create an accurate model.
- Friction can create dead zone regions where the system doesn't respond to actuator input. This study comprehensively analyzed these dead zones, calculating friction across various system components.
- Tension forces in belts play a crucial role in generating dead zones. The interplay between tension and dead zones was investigated, revealing how tension shapes the system's mechanics.
- The simulations facilitate the understanding of how dead zones, tension forces, and system dynamics interact to generate a variable coupled dead zone process in the dynamics of the 2-DoF system. This provided essential required insights into actuator input behavior within and outside of the dead zone boundaries.

In summation, this comprehensive study has not only provided a nuanced comprehension of the CoreXY mechanism's dynamic equations but has also unraveled the intricate threads of friction-induced dead zones and tension force effects, paving the way for enhanced insights into the system's operational dynamics. As the intricate tapestry of the CoreXY mechanism's behavior unravels, this study sets a solid foundation for future endeavors in both analysis and application within the realm of dynamic mechanical systems.

Ongoing future works

In this paper, the kinematics and dynamics of the CoreXY mechanism have been derived under the assumption of belt non-sag around the pulleys. Future work could involve incorporating this consideration into the dynamic equations of the system. Additionally, addressing the motion control or force control of the CoreXY mechanism may pose unique challenges in dealing with dead zones and precise control. These aspects are subjects that will be explored in further investigation.

Data usage

This study does not depend upon any copyright-supported data.

Funding information

This study received no funding.

Conflict of interest

This manuscript includes no potential conflict of interest.

References

- [1] A. Amthor, S. Zschaeck, and C. Ament, "High precision position control using an adaptive friction compensation approach," *IEEE Transactions on Automatic Control*, vol. 55, no. 1, pp. 274-278, 2010.
- [2] J. Shah, B. Snider, T. Clarke, S. Kozutsky, M. Lacki, and A. Hosseini, "Large-scale 3D printers for additive manufacturing: design considerations and challenges," *The International Journal of Advanced Manufacturing Technology*, vol. 104, no. 9-12, pp. 3679-3693, 2019.
- [3] J. O. Jang, "dead zone compensation of an XY-positioning table using fuzzy logic," *IEEE Transactions on Industrial Electronics*, vol. 52, no. 6, pp. 1696-1701, 2005.
- [4] S. He, H. Tang, Z. Zhu, P. Zhang, Y. Xu, and X. Chen, "A novel flexure piezomotor with minimized backward and nonlinear motion effect," *IEEE Transactions on Industrial Electronics*, vol. 69, no. 1, pp. 652-662, 2022.
- [5] M. Yin, Y. Chen, K. H. Lee, D. K. C. Fu, Z. T. Ho Tse, and K. W. Kwok, "Dynamic modeling and characterization of the core-XyCartesian motion system," in 2018 IEEE International Conference on Real-time Computing and Robotics (RCAR), Kandima, Maldives, 2018, pp. 206-211.
- [6] K. S. Sollmann, M. K. Jouaneh, and D. Lavender, "Dynamic modeling of a two-axis, parallel, H-frame-type XY positioning system," *IEEE/ASME Transactions on Mechatronics*, vol. 15, no. 2, pp. 280-290, 2010.
- [7] E. Idà, F. Nanetti, and G. Mottola, "An alternative parallel mechanism for horizontal positioning of a nozzle in an FDM 3D printer," *Machines*, vol. 10, no. 7, pp. 542, 2022.
- [8] M. Miyasaka, M. Haghighipanah, Y. Li, J. Matheson, A. Lewis, and B. Hannaford, "Modeling cable-driven robot with hysteresis and cable-pulley network friction," *IEEE/ASME Transactions on Mechatronics*, vol. 25, no. 2, pp. 1095-1104, 2020.
- [9] L. Yuan, L. Wang, R. Qi, Z. Zhao, J. Jin, and C. Zhao, "A novel hollow-type XY piezoelectric positioning platform," *International Journal of Mechanical Sciences*, vol. 255, pp. 108496, 2023.
- [10] M. R. Homaeinezhad, M. Homaeinezhad, S. Akbari, and D. N. G. Hosseini, "Input-decoupled discrete-time sliding mode control algorithm for servo multi-field multi-armature DC machine," *ISA Transactions*, vol. 127, pp. 283-298, 2022.
- [11] A. Izadbakhsh, N. Nassiri, and M. B. Menhaj, "Linear/nonlinear PID control of cooperative multiple robot manipulators: A robust approach," *AUT Journal of Modeling and Simulation*, vol. 55, no. 1, pp. 71-98, 2023.
- [12] E. Ostertag, N. Bakri, and N. Becker, "Functional disturbance observer for simultaneous control and dry friction

- compensation,” *IFAC Proceedings Volumes*, vol. 22, no. 6, pp. 421-426, 1989.
- [13] H. Ahmadian, I. Sharifi, and H. A. Talebi, “Robust distributed lasso-model predictive control design: A case study on large-scale multi-robot systems,” *AUT Journal of Modeling and Simulation*, vol. 55, no. 1, pp. 127-138, 2023.
 - [14] E. Jahanbazi, F. Jahangiri, and M. R. Mohammadi, “Neural network based fault tolerant LQR control for orbital maneuvering in LEO satellites using hall effect thrusters,” *AUT Journal of Modeling and Simulation*, vol. 55, no. 1, pp. 171-182, 2023.
 - [15] G. S. Mfoumou, G. D. Kenmoé, and T. C. Kofané, “Computational algorithms of time series for stick-slip dynamics and time-delayed feedback control of chaos for a class of discontinuous friction systems,” *Mechanical Systems and Signal Processing*, vol. 119, pp. 399-419, 2019.
 - [16] W. Liu, F. Yang, X. Zhu, and X. Chen, “Stick-slip vibration behaviors of BHA and its control method in highly-deviated wells,” *Alexandria Engineering Journal*, vol. 61, no. 12, pp. 9757-9767, 2022.
 - [17] Q. Huang, Z. Xie, and H. Liu, “Active control for stick-slip behavior of the marine propeller shaft subjected to friction-induced vibration,” *Ocean Engineering*, vol. 268, pp. 113302, 2023.
 - [18] D. Zhang, L. Kong, S. Zhang, Q. Li, and Q. Fu, “Neural networks-based fixed-time control for a robot with uncertainties and input dead zone,” *Neurocomputing*, vol. 390, pp. 139-147, 2020.
 - [19] G. Galuppini, L. Magni, and D. Martino, “Model predictive control of systems with dead zone and saturation model predictive control of systems with dead zone and saturation,” *Control Engineering Practice*, vol. 78, pp. 56-64, 2018.
 - [20] M. Ebrahimi and M. Homaeinezhad, “Compensation of friction and stick-slip uncertainties in trajectory tracking control of servo DC machines considering actuation constraints,” *Proceedings of the Institution of Mechanical Engineers, Part I: Journal of Systems and Control Engineering*, vol. 238, no. 3, pp. 479-503, 2024.
 - [21] M. R. Homaeinezhad and M. M. Ebrahimi, “Tracking control stabilization of systems manipulated by constrained parabolic nonlinear actuator,” *International Journal of Dynamics and Control*, pp. 1-18, 2024.